Proliferation of amyloid-β42 aggregates occurs through a secondary nucleation mechanism

Samuel I. A. Cohen[a], Sara Linse[b,1], Leila M. Luheshi[a], Erik Hellstrand[b], Duncan A. White[a], Luke Rajah[a], Daniel E. Otzen[c], Michele Vendruscolo[a], Christopher M. Dobson[a,1], and Tuomas P. J. Knowles[a,1]

[a]Department of Chemistry, University of Cambridge, Cambridge CB2 1EW, United Kingdom; [b]Department of Biochemistry and Structural Biology, Lund University, SE221 00 Lund, Sweden; and [c]Interdisciplinary Nanoscience Center (iNANO), Centre for Insoluble Structures (inSPIN) and Department of Molecular Biology and Genetics, Aarhus University, 8000 Aarhus C, Denmark

Edited* by William A. Eaton, National Institute of Diabetes and Digestive and Kidney Diseases, National Institutes of Health, Bethesda, MD, and approved April 12, 2013 (received for review October 22, 2012)

The generation of toxic oligomers during the aggregation of the amyloid-β (Aβ) peptide Aβ42 into amyloid fibrils and plaques has emerged as a central feature of the onset and progression of Alzheimer's disease, but the molecular pathways that control pathological aggregation have proved challenging to identify. Here, we use a combination of kinetic studies, selective radiolabeling experiments, and cell viability assays to detect directly the rates of formation of both fibrils and oligomers and the resulting cytotoxic effects. Our results show that once a small but critical concentration of amyloid fibrils has accumulated, the toxic oligomeric species are predominantly formed from monomeric peptide molecules through a fibril-catalyzed secondary nucleation reaction, rather than through a classical mechanism of homogeneous primary nucleation. This catalytic mechanism couples together the growth of insoluble amyloid fibrils and the generation of diffusible oligomeric aggregates that are implicated as neurotoxic agents in Alzheimer's disease. These results reveal that the aggregation of Aβ42 is promoted by a positive feedback loop that originates from the interactions between the monomeric and fibrillar forms of this peptide. Our findings bring together the main molecular species implicated in the Aβ aggregation cascade and suggest that perturbation of the secondary nucleation pathway identified in this study could be an effective strategy to control the proliferation of neurotoxic Aβ42 oligomers.

chemical kinetics | molecular mechanisms | protein misfolding | neurodegeneration

The 42-residue amyloid-β (Aβ) peptide, Aβ42, has been identified as a central constituent in the molecular pathways that underlie Alzheimer's disease (AD) (1–6) through the generation of low molecular weight oligomers from this normally soluble peptide (2, 7–9). The highly complex self-assembly behavior exhibited by this peptide has, however, prevented its mechanism of aggregation from being defined in terms of molecular events in the manner that has been possible for other biomolecular assemblies, such as actin (10) and some prions (11, 12). Particular attention has been devoted to the study of oligomers, which are small multimers that do not yet possess the ability to elongate at the same rate as fibrils and are commonly associated with neuronal death both in vivo and in vitro (2, 7–9). The relationship between low molecular weight toxic oligomers and the mature fibrils has remained elusive, with some studies suggesting that oligomers are generated predominantly as on-pathway intermediates in fibril formation and others indicating that these different species originate mainly from independent pathways (13). Here, we connect the characteristic macroscopic features of Aβ42 fibril formation to their microscopic determinants through the analysis of experimental kinetic data in terms of microscopic rate laws and use selective radiolabeling, size-exclusion chromatography, and cell viability studies to define the origin of the toxic oligomers and their relationship with fibrillar aggregates. We uncover a close connection between the monomeric peptide, the toxic oligomeric species, and the mature fibrils by showing that after a small but critical concentration of amyloid fibrils has formed, the toxic oligomers are predominantly generated from the monomeric peptide in a secondary nucleation reaction that is catalyzed very strongly by the larger fibrillar species.

To elucidate the dominant mechanisms of aggregate proliferation, we focus first on the fibril population detected in thioflavin T (ThT) fluorescence experiments (Figs. 1–3). Because the nucleation pathways proceed through oligomeric intermediates, the information that we obtain from this kinetic analysis can also be used to predict the mechanisms for on-pathway oligomer formation. In the second part of this paper, we verify these predictions explicitly through isolating oligomeric fractions by means of chromatography and show that the overall generation of oligomers is an integral part of the Aβ secondary nucleation mechanism (Figs. 4 and 5).

Results and Discussion

Microscopic Mechanisms. The general method underlying the kinetic analysis builds on earlier work (10, 14–17, 18, 19, 21, 22) and considers all of the possible sources of new aggregates, which consist of two or more monomers, from the species present in the system, as shown in Table 1, from both primary (10, 19, 23–25) and secondary (11, 12, 14, 26–28) pathways. Primary pathways, such as homogeneous nucleation (10, 19), generate new aggregates at a rate dependent on the concentration of monomers alone and independent of the concentration of existing fibrils. Secondary pathways are the complementary class of mechanisms that generate new aggregates at a rate dependent on the concentration of existing fibrils. The latter class can be subdivided into monomer-independent processes, such as fragmentation (11, 12, 18, 26), with a rate depending only upon the concentration of existing fibrils, and monomer-dependent processes, such as secondary nucleation (14, 22, 27, 28), where the surfaces of existing fibrils catalyze the nucleation of new aggregates from the monomeric state, with a rate dependent on both the concentration of monomers and that of existing fibrils. Together, these three classes of mechanism, shown in Table 1, form the basis of a general description of protein aggregation (15, 17), because they account for the generation of new aggregates from mechanisms that involve monomers alone, existing aggregates alone, or both monomers and existing aggregates. These pathways initially populate oligomeric intermediates (29), which lead to fibrillar forms that elongate at a rate that is independent of their length (10, 15, 17) and represent the bulk of the aggregate mass.

Author contributions: S.I.A.C., S.L., L.M.L., E.H., D.E.O., M.V., C.M.D., and T.P.J.K. designed research; S.I.A.C., S.L., L.M.L., E.H., and T.P.J.K. performed research; S.L. contributed new reagents/analytic tools; S.I.A.C., S.L., L.M.L., E.H., D.A.W., L.R., M.V., C.M.D., and T.P.J.K. analyzed data; and S.I.A.C., S.L., E.H., M.V., C.M.D., and T.P.J.K. wrote the paper.

The authors declare no conflict of interest.

*This Direct Submission article had a prearranged editor.

[1]To whom correspondence may be addressed. E-mail: Sara.Linse@biochemistry.lu.se, cmd44@cam.ac.uk, or tpjk2@cam.ac.uk.

This article contains supporting information online at www.pnas.org/lookup/suppl/doi:10.1073/pnas.1218402110/-/DCSupplemental.

Table 1. Schema of the general processes that create new aggregates (14, 15)

	←Primary pathways→		←Secondary pathways→			
			←Monomer-independent→		←Monomer-dependent→	
The general classes of mechanism that create new aggregates	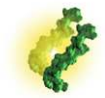		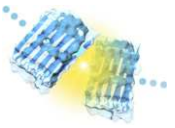		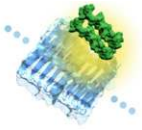	
Mechanism involves	Monomers **only**		Fibrils **only**		**Both** monomers **and** fibrils	
Example	Homogeneous nucleation		Fragmentation		Secondary nucleation	
Early time dependence $M(t)/M(\infty) \sim$	Polynomial $(\lambda t)^2$	✗	Exponential $\exp(\kappa t)$	✓	Exponential $\exp(\kappa t)$	✓
Overall reaction monomer dependence	Strong $t_{\mathrm{lag}} \propto \lambda^{-1} \propto m(0)^{-\frac{n_c}{2}}$	✓	Weak $t_{\mathrm{lag}} \propto \kappa^{-1} \propto m(0)^{-\frac{1}{2}}$	✗	Strong $t_{\mathrm{lag}} \propto \kappa^{-1} \propto m(0)^{-\frac{n_2+1}{2}}$	✓
Agreement with data	Fig. 1B	✗	Fig. 1C	✗	Fig. 1D	✓

Check marks and crosses denote whether or not the characteristics of each mechanism match the data in Fig. 1. The fibril structure is adapted from ref. 20.

Linear Theory. These three classes of mechanism, summarized in Table 1, exhibit qualitatively different features, both as a function of time and as a function of the initial monomer concentration (14, 15, 18, 30). These differences are readily observed by considering the behavior of the system for early times before appreciable amounts of monomer have been sequestered into aggregates (15) when the rate equations can be linearized (15, 30). For cases where the mechanism that creates aggregates involves the preexisting fibrils, such as fragmentation or secondary nucleation, positive feedback for the increase of the fibril mass concentration, $M(t)$, results in the evolution of the form (14, 18) $d^2M(t)/dt^2 = \kappa^2 M$, and hence exponential growth $M(t) \sim \exp(\kappa t)$ is observed, leading to a strong lag phase (14, 15, 17). The duration of the lag phase is commonly described by a lag time t_{lag}, defined as the time at which the aggregate concentration reaches a small fixed percentage of the total peptide concentration. Here, $\kappa = \sqrt{2k_+k_2m^{n_2+1}}$ is the combined parameter that controls proliferation through secondary pathways, k_2 is the rate constant for the secondary process, m is the monomer concentration, k_+ is the fibril elongation rate constant, and n_2 is the reaction order of the secondary pathway with respect to the monomer (15, 30). By contrast, for cases where nucleation is independent of the fibril concentration, such as for classical homogeneous nucleation (10), no feedback is generated, $d^2M(t)/dt^2 = \lambda^2$, and hence slow polynomial growth results, $M(t) \sim \lambda^2 t^2$, with a weak lag phase (10, 15, 30), where $\lambda = \sqrt{2k_+k_nm^{n_c}}$ is the combined parameter controlling proliferation through primary nucleation, k_n denotes the primary nucleation rate constant, and n_c is the reaction order of the primary process (10, 15, 30). The reaction orders n_c and n_2 need not correspond to structural sizes of nuclei (30). The distinction between polynomial growth for primary processes and exponential-type growth for secondary processes is in general maintained for more complicated pathways, such as cascades through multiple intermediates (15, 30, 31).

A second distinction between the basic mechanisms in Table 1 is whether or not the monomer concentration affects the process. If it does, a high concentration dependence of the lag time is possible, otherwise only a weak dependence emerges because a change in the monomer concentration has no direct effect on the nucleation pathway. It is convenient to describe the monomer dependence of the overall assembly reaction, including elongation-related processes, with a power-law relationship, $t_{\mathrm{lag}} \sim m(0)^{\gamma}$, which relates the lag time t_{lag} for the reaction to the initial peptide concentration $m(0)$ (15, 30). The exponent γ in the power law for the lag time (14, 15) is to a good approximation defined by the monomer dependence of the combined parameter λ in the case where primary pathways are dominant and from κ in the case of secondary pathways. In this manner, the exponent is given from λ as $\gamma = -n_c/2$ for processes where a classical homogeneous nucleation step is the major source of aggregates (10) and from κ as $\gamma = -(n_2+1)/2$ for phenomena where secondary nucleation processes dominate (14, 17). A strong monomer dependence, $|\gamma| \geq 1$, can, therefore, always be captured by either primary or secondary nucleation through an appropriate value of n_c or n_2. By contrast, monomer-independent secondary processes, such as fragmentation, are associated with a weaker overall monomer scaling (16, 18) corresponding to a monomer reaction order $n_2 = 0$, $\gamma = -1/2$, with this remaining weak monomer

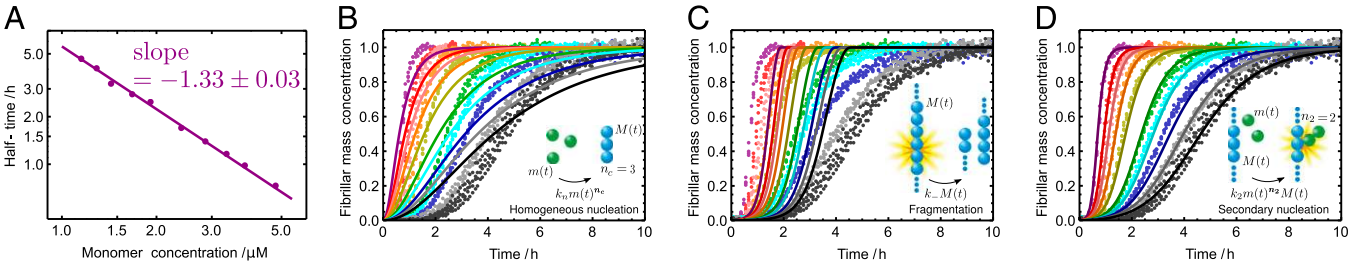

Fig. 1. Experimental kinetics of Aβ42 aggregation under quiescent conditions for 10 initial monomer concentrations. (*A*) Power-law scaling of the time to half-completion with the initial monomer concentration. The slope gives the scaling exponent γ discussed in the text. (*B–D*) Global fits to the normalized experimental data, using the analytical solutions for systems where (*B*) the dominant nucleation mechanism is primary nucleation, and there are no secondary pathways (10, 17); (*C*) a (dominant) fragmentation process is active in addition to primary nucleation (16); and (*D*) secondary nucleation, in addition to primary nucleation, creates new aggregates, Eq. **1** (see *SI Text* for further discussion of these fits). The rate constants are (*B*) $\sqrt{k_+k_n} = 8 \cdot 10^3 \mathrm{M}^{-\frac{3}{2}}\mathrm{s}^{-1}$, with $k_2 = 0$, $n_c = 3$; (*C*) $\sqrt{k_+k_n} = 10\mathrm{M}^{-1}\mathrm{s}^{-1}$, $\sqrt{k_+k_-} = 0.4\mathrm{M}^{-\frac{1}{2}}\mathrm{s}^{-1}$, with $n_c = 2$; and (*D*) $\sqrt{k_+k_n} = 30\mathrm{M}^{-1}\mathrm{s}^{-1}$, $\sqrt{k_+k_2} = 2 \cdot 10^5 \mathrm{M}^{-\frac{3}{2}}\mathrm{s}^{-1}$, with $n_c = n_2 = 2$.

dependence originating only from the fibril elongation step in the overall self-assembly pathway.

Nonlinear Theory. Due to the complexity inherent in amyloid aggregation, it is challenging to acquire data in the regime where the linear solutions are fully valid, because in this early region the signals from bulk assays are low. To extend the applicability of kinetic analysis (14, 15) to amyloid systems, it is therefore desirable to consider the full reaction time course to maximize the constraints on the molecular mechanisms determined from the experimental data (22, 30). At later times in the reaction, as the monomer is consumed, the equations describing the overall assembly process become highly nonlinear and are challenging to integrate (15–17, 18, 22, 30). We have, however, recently derived self-consistent rate laws for the assembly process that are valid for the entire time course of the reaction (22). The full rate law reveals that the same two principal parameters κ and λ, which were identified in the early time behavior (Table 1), define much of the macroscopic behavior in the nonlinear regime also, although the rate laws themselves have a different form, Eq. **1**. An analysis of the full time course, therefore, introduces additional constraints without introducing any additional freedom, resulting in a stringent test of the theory and robust mechanistic conclusions.

Secondary Nucleation Controls Aβ42 Fibril Formation. To obtain a clear picture of the molecular mechanisms that give rise to Aβ42 fibrils, it is essential to generate highly reproducible experimental data reporting on this process. We have been able to collect these types of data at pH values and concentrations of the peptide that relate to physiological conditions (32) by controlling carefully the inertness of surfaces within which solutions of the peptide are contained and by purifying the recombinant monomeric peptide, using repeated applications of size-exclusion chromatography to ensure well-defined initial conditions before initiating kinetic assays (33) (Fig. S1). The kinetics of fibril formation are followed using ThT fluorescence measurements (33), which we have independently verified to be linearly related to the total mass of Aβ42 fibrils under our carefully controlled conditions (Fig. S2).

The value for the scaling exponent, which describes how the lag time or half-time of the reaction scales with the initial concentration of monomer, measured in Fig. 1*A* (and for preseeded growth in Fig. S3) for Aβ42 under quiescent conditions, is $\gamma = -1.33 \pm 0.03$. The lag time and the time to half completion follow the same overall monomer scaling dependence (17, 22) (Table 1), and in this paper we use the half-time because it is available accurately from experimental data. It is interesting to note from Table 1 that this observation of the monomer dependence excludes aggregate fragmentation, believed to be vital, for example, in the propagation of prions (11, 12), as the dominant mechanism driving Aβ42 aggregation, because this process would result in an exponent of $\gamma \approx -0.5$. The value of the scaling exponent is, however, consistent with a dominant secondary nucleation pathway characterized by a monomer dependence of $n_2 = 2$ and a contribution from primary nucleation with a reaction order of $n_c = 2$, the effect of which is to lower the scaling exponent (22) from the value $\gamma = -(n_2 + 1)/2 = -1.5$ toward the value $\gamma = -n_c/2 = -1$ given for proliferation through primary nucleation only. We can now test this conclusion directly by checking explicitly the degree to which the experimental data determined for the full time course of the reaction are matched by the predictions from the rate law, Eq. **1**, when all 10 initial peptide concentrations are used and the only two free parameters, $\sqrt{k_+k_n}$ and $\sqrt{k_+k_2}$ that enter κ and λ, are fixed globally to the same values for all 10 measured peptide concentrations to provide the best fit for the entire dataset consisting of 10 reaction profiles.

The results shown in Fig. 1*D* demonstrate the excellent agreement between the theoretical predictions from Eq. **1** and the experimental data over the full reaction time course under a wide range of concentrations. Moreover, the best fit when the secondary nucleation parameter κ is fixed to zero (Fig. 1*B*) shows that, whereas a description that lacks secondary pathways is able to account approximately for the scaling of the half-time of the reaction with the monomer concentration, it is not able to describe even qualitatively the full time courses observed in the experiments. In particular, the early-stage growth observed in the experimental data is much stronger than the polynomial form associated with primary nucleation and is instead described by the exponential growth associated with secondary pathways (Table 1). A fit to the case where most new aggregates are generated through fragmentation (Fig. 1*C*) is conversely able to account for the exponential growth at early times, but it is not able to match the more than linear monomer dependence of the reaction timescale (Table 1). By contrast, the fit including fibril-catalyzed secondary nucleation (Fig. 1*D*), where the surfaces of fibrils catalyze the nucleation of new aggregates from monomeric peptide (14, 27, 28), describes the entire set of time courses, including the characteristic exponential shape at early times and the monomer scaling, using only two global parameters that are fixed to the same value across all datasets. This result is particularly striking because it shows that the production of new Aβ42 fibrils does not occur predominantly through the classical mechanism of primary nucleation, which initially involves the coalescence of monomeric peptides into oligomers independently of existing fibrils, but occurs by secondary processes that are critically dependent on the latter species. It is interesting to note that the secondary nucleation mechanism identified here for the aggregation of the Aβ42 peptide is formally analogous to that originally identified for the polymerization of sickle hemoglobin (14). In the present case, however, electron microscopy indicates that fibrils are not generally attached to one another at the locations of secondary nucleation events (Fig. S4), implying that secondary nucleated aggregates detach from the fibril surface. Recent atomic force microscopy studies have captured the formation of such nuclei (34).

Rational Alteration of the Aggregation Pathway. A factor that has contributed greatly to previous difficulties in developing a clear picture of Aβ42 aggregation is the high sensitivity of the kinetics of aggregation to even small changes in the reaction conditions. Here, we can use such differences in aggregation behavior in a systematic manner to reveal the underlying microscopic mechanisms. Thus, having shown that Aβ42 aggregation under quiescent conditions is controlled by a fibril-catalyzed secondary nucleation process, we sought to modify the dominant factors determining the aggregation pathway by introducing shear forces through shaking and to identify the signals in the kinetic data that report on this change.

The rate equations (16, 22) lead to the intriguing prediction for Aβ42 that, if such shear gradually introduces fibril fragmentation as a molecular mechanism (Fig. 2), the scaling exponent (16, 22, 30)—relating the lag time or half-time to the monomer concentration—will change monotonically from the quiescent value of −1.33 and approach the theoretical limit of −0.5 (Table 1) associated with fragmentation (16, 22, 30) at very high agitation rates (Fig. 2 *A–E*, *Lower*). Remarkably, the overall effect of fragmentation is incorporated in the rate equations through the introduction of a single additional parameter relative to the quiescent case (*SI Text*), $\sqrt{k_+k_-}$, by use of which we are able to fit very closely the kinetic traces at each agitation rate (Fig. 2 *B–E*, *Upper*). Furthermore, we verified using electron microscopy and seeding experiments that the morphology of the fibrils remained unchanged (Figs. S4 and S5). The global nature of the fit is equivalent to the ability to predict quantitatively the behavior of the system with changes in experimental conditions; such a situation is likely to be found only when the model captures correctly the molecular events taking place in the reaction.

It is interesting to note from Fig. 2 that increasing levels of shear change not only the power law for the half-time, but also the characteristic form of the kinetic profiles at the late stages of the reaction (Fig. 3*A*) (30). A change occurs because fragmentation, unlike secondary nucleation, is not directly affected by the depletion

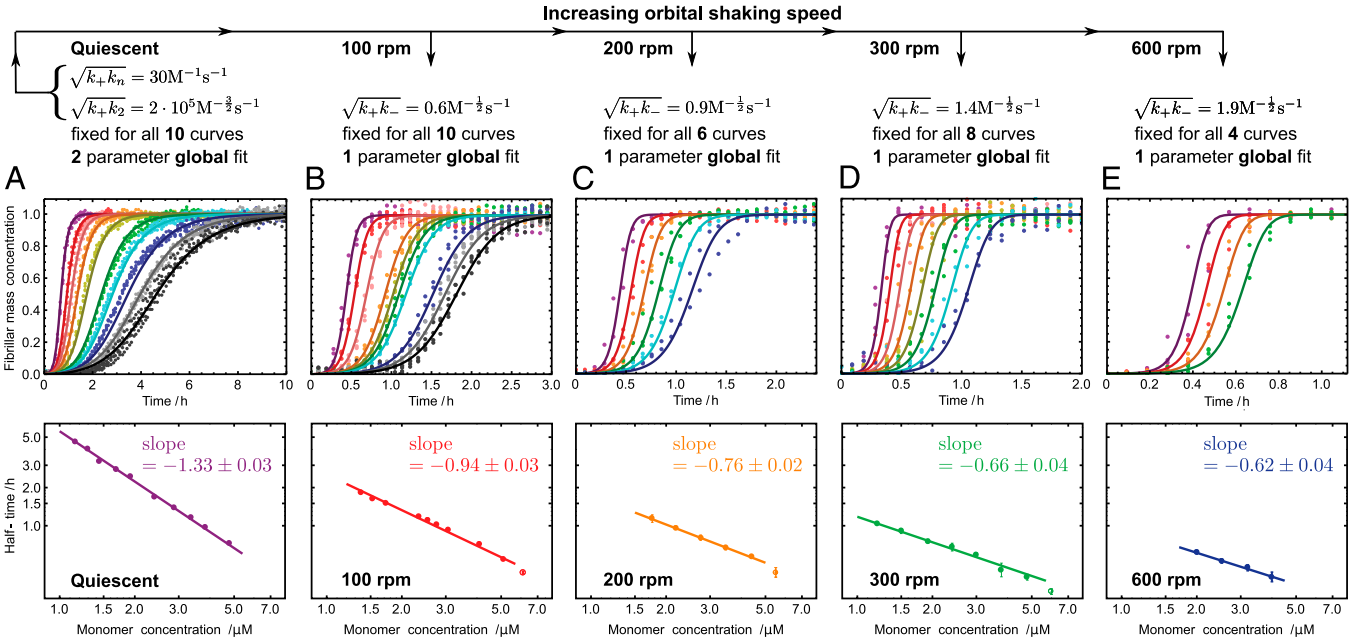

Fig. 2. Experimental kinetics for Aβ42 aggregation under varying levels of shear generated by agitating the sample at different speeds (*Upper*) and the power-law relationships observed between the half-time and the initial monomer concentration (*Lower*). The slopes (*Lower*) give the scaling exponent γ discussed in the text. The two rate parameters determined from the global fit to the data under quiescent conditions (*A, Upper*) are held fixed and all of the normalized experimental profiles (*B–E, Upper*) are fitted with a single additional parameter for each shear rate. Note the different timescales (*Upper*). (*Upper* and *Lower*) The scale on the ordinate is the same. Predicted deviations from the power law at high concentration are shown as open circles (*SI Text*).

of the monomeric peptide toward the end of the reaction. Although both fragmentation and secondary nucleation exhibit exponential growth, $\sim\exp(\kappa t)$, in the early stages of the reaction (Table 1), an expansion of Eq. **1** for late times (22) predicts a sharper, double-exponential approach, $\sim\exp(-\exp(\kappa t))$, to the plateau in the late stages of the reaction at high shear driven by fragmentation, in contrast to a less sharp, $\sim\exp(-\kappa t/\sqrt{3})$, exponential approach for the quiescent reaction driven by monomer-dependent secondary nucleation. In agreement with this prediction, a comparison of two traces at the same initial monomer concentration, under quiescent and high-shear conditions, is shown in Fig. 3*A* and reveals the predicted intricate transformation from an asymmetric curve under quiescent conditions that changes less rapidly toward the end of the reaction than at the beginning to a curve under high-shear conditions that has a sharper approach to the plateau and possesses the opposite asymmetry (30).

Confirming the Source of Oligomer Populations with Radioactive Peptides. The analysis of the kinetic data indicates that a major and continuous source of new fibrils under quiescent conditions is a secondary nucleation mechanism that involves both the monomeric peptide and mature amyloid fibrils. Because a large number of peptides are required to form ordered fibrillar forms that are detected in ThT measurements, aggregates generated through the secondary pathway must initially be in prefibrillar, oligomeric states that can escape detection by this method (24, 35). To observe directly these ThT-invisible oligomer populations, which can ultimately convert to fibrils, and pinpoint their molecular origin, we studied a pair of samples with the same concentration of ^{35}S-radiolabeled peptide, but one containing in addition to the soluble radioactive peptide a small concentration of unlabeled preformed fibrils. We measured the concentration of oligomers in both aggregating samples by quantifying through liquid scintillation assays the radioactivity in the oligomer fractions obtained from size-exclusion chromatography. This highly sensitive method of detecting oligomers has the advantage of not requiring any chemical labels and, therefore, leaves all of the chemical characteristics of the peptide intact.

The data in Fig. 4*A* show that the rate of generation of oligomers is dramatically enhanced in the solution that contains preformed fibrils even though the initial concentration of soluble peptide is kept constant. Crucially, because the added fibrils in these experiments are unlabeled, these results establish that oligomers are formed from the monomeric peptide, but in a reaction that is catalyzed very strongly by the presence of fibrils (Fig. S6). We also carried out the complementary experiments where unlabeled monomers were incubated with radiolabeled fibrils; the data in Fig. 4*A* show that no radioactivity is detectable in the oligomer fraction, confirming that the oligomers do not originate from the preformed fibrils themselves (e.g., through fragmentation or dissociation), but rather are formed from monomers through secondary nucleation. We verified these results using immunochemistry (Fig. 4*B*), by probing the amount of Aβ42 present in the oligomer fractions obtained from size-exclusion chomatography,

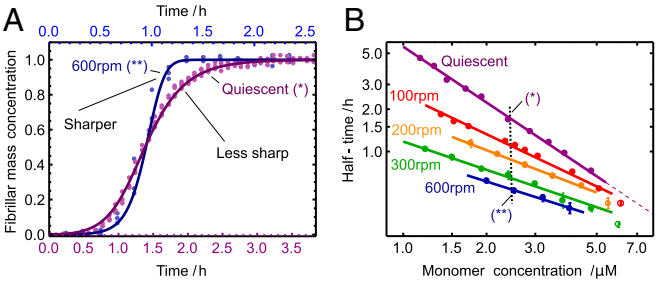

Fig. 3. Shear alters the symmetry of the reaction profile. (*A*) Comparison of the shape of the kinetic profiles under quiescent and high-shear conditions (33), corresponding to concentrations marked *B* with a vertical dotted line. The solid lines are the theoretical rate laws with the rate constants identified in Fig. 2. (*B*) Power-law relationship for the monomer dependence at varying shear rates from Fig. 2 *A–E* (*Lower*). The weakening of the monomer dependence, given by the magnitude of the slope, occurs as fragmentation is gradually introduced as a molecular mechanism. Predicted deviations from the power law at high concentration are shown as open circles (*SI Text*).

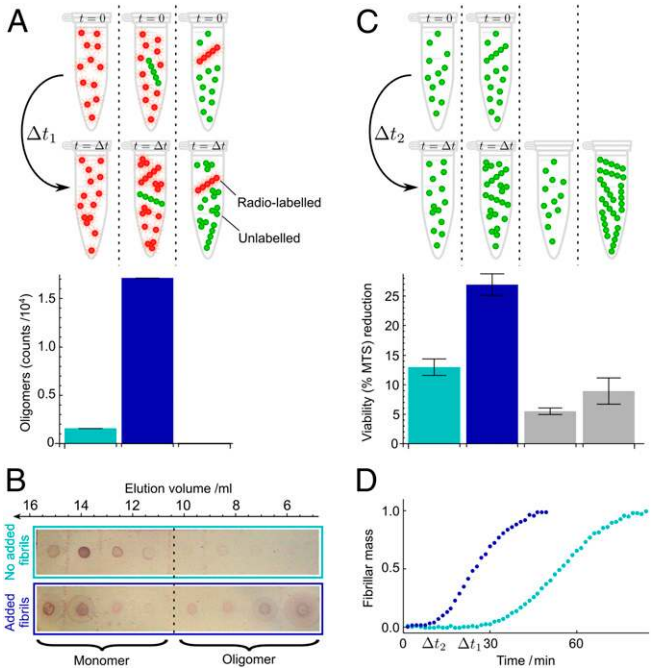

Fig. 4. Direct measurement of oligomer populations, using radioactive Aβ42 peptides. (*A*) Samples of monomer (light blue bar) or monomer mixed with 1% preformed fibrils (dark blue bar and right bar) with selective radiolabeling of monomer or fibrils, as indicated in red, were incubated followed by size-exclusion chromatography and liquid scintillation counting. The counts for the oligomer fractions are shown below the respective samples. The monomer counts are shown in Fig. S7. (*B*) Probing the chromatography fractions with the 6E10 antibody confirms the dramatically enhanced production of small oligomers in the presence of fibrils. Time $\Delta t_1 = 24$ min. (*C*) Reduction in cell viability (MTS) for reactions without (light blue bars) and with (dark blue bars) a small concentration of added fibrils under the same conditions as in *A* and after filtration through a 200-nm filter. Values are averages over nine measurements at $\Delta t_2 = 5; 6; 7$ min. Gray bars are the initial (monomer) and end (fibril) reaction time points. (*D*) Normalized kinetic time courses without (light blue) and with (dark blue) added preformed fibrils that correspond to those in *A*–*C*. The rapid increase in the slope of the assay with preformed fibrils (dark blue) after *ca*. 10 min, before the matched reaction without preformed fibrils (light blue) has generated significant aggregate mass, indicates rapid creation of new aggregates through secondary nucleation (30) (*SI Text*). The concentration of monomeric Aβ42 was 4 μM and the mass concentration of added fibrils was 40 nM.

confirming the formation of oligomers through secondary nucleation in a fibril-dependent manner.

The combination of the kinetic experiments and the detailed analysis of the chromatography fractions reveals that low molecular weight oligomers are formed in a pathway that involves both the monomer and fibrils. A key question, however, is whether the toxicity known to be associated with Aβ42 aggregation can originate from this same pathway. To address this issue, we measured the reduction in viability (Fig. 4*C*) and the increase in cytotoxicity (Fig. S8) of SH-SY5Y human neuroblastoma cells when exposed to oligomers formed as a result of secondary nucleation. We studied two solutions with an identical monomer concentration and, therefore, an identical population of oligomers generated by primary nucleation; marked differences in the resulting toxicity are evident, however, when a small concentration of preformed fibrils was added to one of these solutions to trigger the production of secondary oligomers as shown above. As the fibrils themselves are observed not to give rise to a high level of toxicity, these observations identify specifically that the major source of cytotoxic oligomers results from a process that involves both the monomeric peptide and the fibrils, i.e., secondary nucleation.

Significance and Conclusions

These results establish a general picture for the self-assembly of Aβ42 that brings together all of the species in the aggregation cascade (Fig. 5). Initially, in the absence of fibrils, all oligomers have to be generated through primary pathways because secondary nucleation requires the presence of fibrils. Once a critical concentration of amyloid fibrils has formed, however, secondary nucleation will overtake primary nucleation as the major source of new oligomers and further proliferation becomes exponential in nature (14, 16, 22) due to positive feedback (Fig. 5). The identification of secondary nucleation underlines the importance of elucidating the detailed structures of amyloid fibrils and their surfaces, information that will motivate molecular simulations to determine the origins of their surface-catalytic activity. The critical concentration of fibrils, above which secondary nucleation becomes the dominant mechanism generating new aggregates, is given from the ratio of the primary to secondary nucleation rate constants, $M^* = k_n/k_2$; the parameters obtained in Fig. 1*D* define this concentration to be of the order of 10 nM. A survey of literature values (Tables S1 and S2) shows that the aggregate loads in the brains of patients suffering from AD are much greater than this critical concentration, and hence the results suggest that secondary nucleation is likely to be active under these conditions. It is therefore interesting to speculate that the secondary nucleation process identified in this in vitro study as the origin of the toxicity of Aβ42 aggregation could also play a major role in vivo, even accounting for the fact that differences in the morphological character and accessible surface area of the amyloid fibrils may cause variations in the rate of oligomer formation through secondary nucleation for different plaque loads.

In agreement with this idea, clear signatures of secondary nucleation are apparent in studies of living systems, as a halo of oligomeric Aβ42 aggregates (38) is found to emanate from amyloid plaques; close to plaques, the primary nucleation rate is unaffected, whereas the generation of oligomers through the secondary nucleation pathway is by definition very significantly enhanced. Furthermore, in the vicinity of plaques, dendritic spines have been found to be disrupted in a manner that depends on their distance from the plaques (39), an observation that suggests that the latter structures are not toxic by themselves in vivo but instead facilitate the generation of toxic oligomers by surface catalysis. The molecular picture that emerges from the present study, therefore, provides a mechanism by which the accumulation of amyloid fibrils is coupled to the generation of low molecular weight diffusive aggregates from monomeric peptide, thereby connecting together all of the main components in the Aβ cascade. This conclusion suggests that an important approach for suppressing the production of neurotoxic Aβ42 oligomers could be to focus on altering the secondary, rather than (or in addition to) the primary, nucleation pathway. Indeed, once the critical concentration of fibrils is exceeded, further perturbation of the primary nucleation pathway ceases to be effective in reducing the overall profileration of oligomers, as most new aggregates are not created via this mechanism.

Materials and Methods

Additional information can be found in *SI Text*.

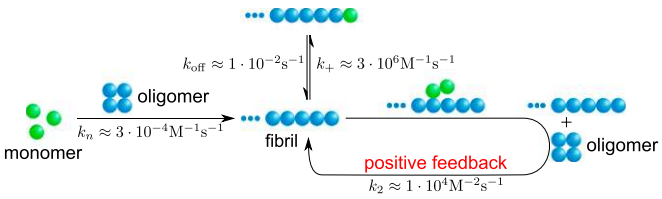

Fig. 5. Schematic showing the overall reaction pathway and the corresponding rate constants identified in this paper. The approximate rates of the elongation-related processes have been identified in previous work (33, 35, 36).

Integrated Rate Law. When both primary and secondary pathways are active, the integrated rate law describing the generation of total fibril mass, $M(t)$, over time as a function only of the initial conditions and the rate constants of the system is given as (16, 22)

$$\frac{M(t)}{M(\infty)} = 1 - \left(\frac{B_+ + C_+}{B_+ + C_+ e^{\kappa t}} \, \frac{B_- + C_+ e^{\kappa t}}{B_- + C_+} \right)^{\frac{k_\infty^2}{\kappa k_\infty}} e^{-k_\infty t}. \quad [1]$$

Although many distinct parameters, including microscopic rate constants for primary nucleation (k_n), elongation (k_+), depolymerization (k_{off}), fragmentation (k_-), and fibril-catalyzed secondary nucleation (k_2), are required to capture the complete assembly process (16, 22), only two particular combinations of the rate constants define much of the macroscopic behavior; these parameters are related to the rate of formation of new aggregates through primary pathways $\lambda = \sqrt{2k_+ k_n m(0)^{n_c}}$ and through secondary pathways $\kappa = \sqrt{2k_+ k_2 m(0)^{n_2+1}}$, where $k_2 = k_-$ when $n_2 = 0$. Indeed, Eq. **1** depends on the rate constants through these two parameters, λ and κ, alone because $B_\pm = (k_\infty \pm \tilde{k}_\infty)/(2\kappa)$, $C_\pm = \pm\lambda^2/(2\kappa^2)$, $k_\infty = \sqrt{2\kappa^2/[n_2(n_2+1)] + 2\lambda^2/n_c}$, and $\tilde{k}_\infty = \sqrt{k_\infty^2 - 4C_+C_-\kappa^2}$. The initial concentration of soluble monomers is $m(0)$ and the reaction orders describing the dependencies of the primary and secondary pathways on the monomer concentration are n_c and n_2.

Materials. We expressed in *Escherichia coli* and purified, as described previously (40), the Aβ(M1–42) peptide (MDAEFRHDSGYEVHHQKLVFFAEDVGSNKGAIIGLMVGGVVIA). Radiolabeled Aβ42 was expressed and purified in the same way, except that cells were grown in minimal medium supplemented with [^{35}S]methionine 2 min before induction. Aliquots of purified Aβ42 were thawed and subjected to gel filtration on a Superdex 75 column in 20 mM sodium phosphate buffer, pH 8, 200 μM EDTA 0.02% NaN_3.

Radiolabeling and Immunochemistry. The peptide samples were taken from an ongoing seeded or unseeded aggregation reaction (Fig. 4) and immediately loaded into a 1 × 30-cm Superdex 75 column. Eluted fractions (2 mL) were diluted 1:4 in scintillation solution (Ready Safe liquid Scintillation Mixture; Beckman Coulter) and placed in a scintillator (Beckman LS6000IC) for counting for a total of 120 min per sample. The counts for fractions with average elution volumes of 6, 8, and 10 mL were binned as oligomer counts (sum of 3- to 20-mer, because the dominant monomer peak makes dimer quantification inaccurate) and counts for fractions eluting at 12, 14, and 16 mL were binned as monomer counts. The experiments were repeated with unlabeled species, and 1-mL eluted fractions were concentrated by lyophilization, dissolved in 8 M urea, and applied to a PVDF membrane for semiquantitative analysis using 6E10 primary antibody (Signet) and alkaline phosphatase-conjugated rabbit anti-mouse secondary antibody (Dako).

Cytotoxicity and Cell Viability Assays. Assays were performed on SH-SY5Y human neuroblastoma cells cultured under standard conditions. The peptide samples were taken from ongoing seeded or unseeded reactions and subjected to filtration through a 200-nm filter (Anapour). Control peptide, monomer, and fibril were not filtrated. Buffer controls were both filtrated and unfiltrated. The cells were then cultured in the presence of the peptides, buffer, or media for a further 24 h before the cytotoxicity and viability assays were performed. Caspase-3/7 activity was measured using the Apo-ONE Homogeneous Caspase-3/7 assay (Promega). Cell viability was measured using the Cell Titer 96 Aqueous One MTS reagent (Promega).

ACKNOWLEDGMENTS. We thank Dale Schenk, Daan Frenkel, and David Chandler for useful discussions. We acknowledge financial support from the Newman Foundation (T.P.J.K.), the Schiff Foundation (S.I.A.C.), the Kennedy Memorial Trust (S.I.A.C.), the Swedish Research Council (S.L.) and its Linneaus Centre Organizing Molecular Matter (S.L. and E.H.), the Crafoord Foundation (S.L.), the Royal Physiographic Society (E.H.), the Nanometer Structure Consortium at Lund University (S.L.), Alzheimerfonden (S.L.), Danish Research Foundation (D.E.O.), and the Wellcome Trust (M.V., C.M.D., and T.P.J.K.).

1. Selkoe DJ (2003) Folding proteins in fatal ways. *Nature* 426(6968):900–904.
2. Haass C, Selkoe DJ (2007) Soluble protein oligomers in neurodegeneration: Lessons from the Alzheimer's amyloid beta-peptide. *Nat Rev Mol Cell Biol* 8(2):101–112.
3. Aguzzi A, Haass C (2003) Games played by rogue proteins in prion disorders and Alzheimer's disease. *Science* 302(5646):814–818.
4. Dobson CM (2003) Protein folding and misfolding. *Nature* 426(6968):884–890.
5. Tanzi RE, Bertram L (2005) Twenty years of the Alzheimer's disease amyloid hypothesis: A genetic perspective. *Cell* 120(4):545–555.
6. Eisele YS, et al. (2010) Peripherally applied Abeta-containing inoculates induce cerebral beta-amyloidosis. *Science* 330(6006):980–982.
7. Kayed R, et al. (2003) Common structure of soluble amyloid oligomers implies common mechanism of pathogenesis. *Science* 300(5618):486–489.
8. Walsh DM, et al. (2002) Naturally secreted oligomers of amyloid beta protein potently inhibit hippocampal long-term potentiation in vivo. *Nature* 416(6880):535–539.
9. Bucciantini M, et al. (2002) Inherent toxicity of aggregates implies a common mechanism for protein misfolding diseases. *Nature* 416(6880):507–511.
10. Oosawa F, Asakura S (1975) *Thermodynamics of the Polymerization of Protein*. (Academic, Waltham, MA).
11. Collins SR, Douglass A, Vale RD, Weissman JS (2004) Mechanism of prion propagation: Amyloid growth occurs by monomer addition. *PLoS Biol* 2(10):e321.
12. Tanaka M, Collins SR, Toyama BH, Weissman JS (2006) The physical basis of how prion conformations determine strain phenotypes. *Nature* 442(7102):585–589.
13. Schnabel J (2011) Amyloid: Little proteins, big clues. *Nature* 475(7355):S12–S14.
14. Ferrone FA, Hofrichter J, Eaton WA (1985) Kinetics of sickle hemoglobin polymerization. II. A double nucleation mechanism. *J Mol Biol* 183(4):611–631.
15. Ferrone F (1999) Analysis of protein aggregation kinetics. *Methods Enzymol* 309:256–274.
16. Knowles TPJ, et al. (2009) An analytical solution to the kinetics of breakable filament assembly. *Science* 326(5959):1533–1537.
17. Cohen SIA, et al. (2011) Nucleated polymerization with secondary pathways. I. Time evolution of the principal moments. *J Chem Phys* 135(6):065105.
18. Bishop MF, Ferrone FA (1984) Kinetics of nucleation-controlled polymerization. A perturbation treatment for use with a secondary pathway. *Biophys J* 46(5):631–644.
19. Oosawa F, Kasai M (1962) A theory of linear and helical aggregations of macromolecules. *J Mol Biol* 4:10–21.
20. Lührs T, et al. (2005) 3D structure of Alzheimer's amyloid-beta(1-42) fibrils. *Proc Natl Acad Sci USA* 102(48):17342–17347.
21. Eaton WA, Hofrichter J (1990) Sickle cell hemoglobin polymerization. *Adv Protein Chem* 40:63–279.
22. Cohen SIA, Vendruscolo M, Dobson CM, Knowles TPJ (2011) Nucleated polymerization with secondary pathways. II. Determination of self-consistent solutions to growth processes described by non-linear master equations. *J Chem Phys* 135(6):065106.
23. Jarrett JT, Lansbury PT, Jr. (1993) Seeding "one-dimensional crystallization" of amyloid: A pathogenic mechanism in Alzheimer's disease and scrapie? *Cell* 73(6):1055–1058.
24. Serio TR, et al. (2000) Nucleated conformational conversion and the replication of conformational information by a prion determinant. *Science* 289(5483):1317–1321.
25. Kar K, Jayaraman M, Sahoo B, Kodali R, Wetzel R (2011) Critical nucleus size for disease-related polyglutamine aggregation is repeat-length dependent. *Nat Struct Mol Biol* 18(3):328–336.
26. Wegner A (1982) Spontaneous fragmentation of actin filaments in physiological conditions. *Nature* 296(5854):266–267.
27. Ruschak AM, Miranker AD (2007) Fiber-dependent amyloid formation as catalysis of an existing reaction pathway. *Proc Natl Acad Sci USA* 104(30):12341–12346.
28. Cacciuto A, Auer S, Frenkel D (2004) Onset of heterogeneous crystal nucleation in colloidal suspensions. *Nature* 428(6981):404–406.
29. Cremades N, et al. (2012) Direct observation of the interconversion of normal and toxic forms of α-synuclein. *Cell* 149(5):1048–1059.
30. Cohen SIA, Vendruscolo M, Dobson CM, Knowles TPJ (2012) From macroscopic measurements to microscopic mechanisms of protein aggregation. *J Mol Biol* 421(2–3):160–171.
31. Flyvbjerg H, Jobs E, Leibler S (1996) Kinetics of self-assembling microtubules: An "inverse problem" in biochemistry. *Proc Natl Acad Sci USA* 93(12):5975–5979.
32. Hu X, et al. (2009) Amyloid seeds formed by cellular uptake, concentration, and aggregation of the amyloid-beta peptide. *Proc Natl Acad Sci USA* 106(48):20324–20329.
33. Hellstrand E, Boland B, Walsh DM, Linse S (2010) Amyloid β-protein aggregation produces highly reproducible kinetic data and occurs by a two-phase process. *ACS Chem Neurosci* 1(1):13–18.
34. Jeong JS, Ansaloni A, Mezzenga R, Lashuel HA, Dietler G (2013) Novel Mechanistic Insight into the Molecular Basis of Amyloid Polymorphism and Secondary Nucleation during Amyloid Formation. *J Mol Biol* 10.1016/j.jmb.2013.02.005.
35. Lee J, Culyba EK, Powers ET, Kelly JW (2011) Amyloid-β forms fibrils by nucleated conformational conversion of oligomers. *Nat Chem Biol* 7(9):602–609.
36. Buell AK, et al. (2012) Detailed analysis of the energy barriers for amyloid fibril growth. *Angew Chem Int Ed Engl* 51(21):5247–5251.
37. Sánchez L, et al. (2011) Aβ40 and Aβ42 amyloid fibrils exhibit distinct molecular recycling properties. *J Am Chem Soc* 133(17):6505–6508.
38. Koffie RM, et al. (2009) Oligomeric amyloid beta associates with postsynaptic densities and correlates with excitatory synapse loss near senile plaques. *Proc Natl Acad Sci USA* 106(10):4012–4017.
39. Spires-Jones TL, et al. (2009) Passive immunotherapy rapidly increases structural plasticity in a mouse model of Alzheimer disease. *Neurobiol Dis* 33(2):213–220.
40. Walsh DM, et al. (2009) A facile method for expression and purification of the Alzheimer's disease-associated amyloid beta-peptide. *FEBS J* 276(5):1266–1281.

Supporting Information

Cohen et al. 10.1073/pnas.1218402110

SI Materials and Methods

All chemicals were of analytical grade. The amyloid-β Aβ(M1-42) peptide (MDAEFRHDSGYEVHHQKLVFFAEDVGSNKGAIIGLMVGGVVIA) was expressed in *Escherichia coli* and purified as described previously (1). In short, the purification procedure involved sonication of *E. coli* cells, dissolution of inclusion bodies in 8 M urea, ion exchange in batch mode on DEAE cellulose resin, centrifugation through a molecular weight cutoff (MWCO) of 30,000 filter and, finally, concentration using a MWCO of 3,000 filter. The purified peptide was frozen as identical 1-mL aliquots. Radiolabeled Aβ(M1–42) was expressed and purifed in the same way, except that cells were grown in minimal medium that was supplemented with [^{35}S] methionine 2 min before induction.

Preparation of Samples for Kinetic Experiments. For kinetic experiments, aliquots of puried Aβ42 were thawed and subjected to two rounds of gel filtration on a Superdex 75 column in 20 mM sodium phosphate buffer, pH 8, with 200 μM EDTA and 0.02% NaN_3. The latter part of the monomer peak, Fig. S1, was collected on ice and was typically found to have a concentration (determined by quantitative amino acid analysis purchased from BMC Uppsala) of 5–12 μM. The gel fitration step removes traces of preexistent aggregates and exchanges the buffer for the one used in the fibril formation experiments. The monomer generated in this way was supplemented with 6 μM thioflavin T (ThT) from a 1.2-mM stock and was used to prepare by dilution a series of samples of concentrations between 0.5 and 6 μM Aβ(M1–42) in 20 mM sodium phosphate buffer, pH 8, with 200 μM EDTA and 0.02% NaN_3; before dilution, the solutions were also supplemented with 6 μM ThT so that all samples contain the same ThT concentration. The dilutions were made in low-bind Eppendorff tubes (Axygen) on ice, using careful pipetting to avoid introduction of air bubbles. Each sample was then pipetted into multiple wells of a 96-well half-area plate of black polystyrene with a clear bottom and PEG coating (Corning 3881), 100 μL per well. The samples were added to the plate from lower to higher concentration, after which the plate was sealed with a plastic film (Corning 3095).

Kinetic Assays. Assays were initiated by placing the 96-well plate at 37 °C and shaking at the designated orbital speed in a plate reader (Fluostar Omega or Fluostar Optima; BMGLabtech). The ThT fluorescence was measured through the bottom of the plate every 343 s (with an excitation filter of 440 nm and an emission filter of 480 nm) with continuous shaking (when relevant) between measurements. Each reading lasted for 43 s and the intervening shaking (or quiescent) period lasted for 300 s. The ThT fluorescence was followed for 3–5 repeats of each monomer concentration. The formation of fibrils was verified using transmission electron microscopy (1).

Preseeded Kinetic Assays. Kinetic experiments were set up as above for multiple samples of Aβ42 in 20 mM sodium phosphate buffer, pH 8, with 200 μM EDTA, 6 μM ThT, and 0.02% NaN_3. The ThT fluorescence was monitored for 1.5 h to verify the formation of fibrils. The samples were then collected from the wells into low-bind Eppendorff tubes (Axygen) and sonicated for 2 min in a sonicator bath at room temperature. Fresh monomer was isolated by gel filtration as above and a dilution series prepared in 20 mM sodium phosphate, pH 8, containing 200 μM EDTA, 6 μM ThT, 0.02% NaN_3. For each concentration of freshly prepared monomer, samples were prepared containing the sonicated seeds at concentrations corresponding to 0, 0.04, 0.2, 1, and 30% of the highest monomer concentration in the dilution series, and the ThT fluorescence was monitored in the plate reader every 60 s under quiescent conditions at 37 °C.

Calibration of Thioflavin T Assay. Following our previous work (2), we established the relationship between ThT fluorescence intensity and Aβ42 aggregate mass concentration under our carefully controlled conditions by carrying out several control experiments (Fig. S2). In particular, we observed that the fluorescence intensity from ThT at the end of aggregation reactions scales linearly with the total Aβ42 peptide concentration in the system (Fig. S2*A*). Because these fluorescence values correspond to a system where almost all of the peptide is in aggregated form (2), this control demonstrates that the fluorescence from ThT is linearly related to the Aβ42 aggregate mass concentration.

Furthermore, in a second control, we used radiolabeled peptide coupled to liquid scintillation experiments to determine directly the initial monomer concentration in an aggregating reaction and also the free monomer concentration at the half-time of the same aggregation reaction as indicated by the ThT reaction profile. This measurement, shown in Fig. S2*B*, confirmed that at the half-time indicated by the ThT assay, precisely half of the total monomer in the system did indeed remain as free monomer. These control experiments verify explicitly the faithfulness of ThT as a reporter of Aβ42 aggregate mass concentration in our kinetic studies.

It is interesting to reconcile the robust linear relationship between ThT fluorescence and the total aggregate mass and free monomer concentrations with the fact that ThT reports on fibrillar species. As discussed in the main text, a component of the total aggregate mass that corresponds to low molecular weight aggregates not yet of fibrillar structure may, therefore, not be detected in bulk measurements made using ThT. Importantly, the direct contribution to the aggregate mass concentration due to these ThT-invisible oligomers during the aggregation reaction is observed by radiolabeling experiments, through comparing the radiocounts in Fig. 4*A* and Fig. S7, to be no more than around 1% of the total protein mass in the system. Oligomers are therefore not a significant component of the total aggregate concentration when weighted by mass. The combination of our ThT and radiolabeling measurements shows directly that, at the half-time of the reaction, approximately half of the protein mass remains in the monomeric state, approximately half is in fibrillar form, and only a small fraction is present as oligomers. Measurements of the mass concentration of fibrillar species via ThT fluorescence are hence equal to those of the total aggregate mass concentration, which includes also oligomeric species, to within around 1%, as shown in Fig. S2. This conclusion is equivalent to the statement that $M(t) + m(t) \approx m_{\mathrm{tot}}$, where $M(t)$ is the fibrillar mass concentration, $m(t)$ is the free monomer concentration, and m_{tot} is the total concentration of peptide in the closed system.

Kinetic Data Presentation. The fractional fibrillar mass concentration was calculated from the ThT fluorescence measurements, using the result from our calibration experiments that the two are linearly related. The kinetic traces in Figs. 1 and 2 display the results of three to five replicates overlaid to present transparently the high reproducibility and low spread in the data. Where error bars are shown elsewhere, they are SEs determined from the results of three to five replicates at each concentration. At least two identical plates of 96 solutions were examined at each shaking speed and at quiescent conditions.

Transmission Electron Microscopy. Transmission electron microscopy (TEM) images were acquired using a Philips CM120 BioTWIN electron microscope equipped with a postcolumn energy filter (Gatan GIF100) and a CCD camera. The acceleration voltage was 120 kV. A carbon-coated formvar grid was placed upside down on a droplet of each sample, followed by a quick rinse and then placing the grid upside down on a droplet of 1.5% (wt/vol) uranyl acetate (3). TEM images were taken for samples at quiescent condition at zero time; at 15, 30, and 45 min into the lag phase; and after reaching the equilibrium plateau; and for samples shaken at 100, 200, 300, and 600 rpm after reaching the equilibrium plateau.

Analysis of Monomer and Oligomer Populations Using Radiolabel and Monoclonal Antibodies. Aggregation was monitored by ThT fluorescence for samples of 5 μM Aβ42 with and without 50 nM of preformed seeds in 20 mM sodium phosphate buffer, pH 8, with 200 μM EDTA and 0.02% NaN_3 with 6 μM ThT. Samples with ^{35}S Aβ42 were supplemented with seeds formed from unlabeled peptide, and samples of unlabeled Aβ42 monomer were supplemented with seeds formed from [^{35}S]Aβ42. The aggregation process was monitored until the time point marked $t = \Delta t_1$ in Fig. 4*D*, i.e., the time when the ThT fluorescence intensity of seeded samples has reached 50% of the maximum value and unseeded samples are still in the lag phase. The samples were collected from the wells and immediately injected into a 1 × 30-cm Superdex 75 column. Eluted fractions (2 mL per fraction) were diluted 1:4 in scintillation solution (Ready Safe Liquid Scintillation Mixture; Beckman Coulter) and placed in a scintillator (Beckman LS6000IC) for counting for a total of 120 min per sample. All samples were counted in sequence, 10 min per sample, and 12 such sequences were performed. The counts for fractions eluting at 6, 8, and 10 mL were binned as oligomer counts and counts for fractions eluting at 12, 14, and 16 mL were binned as monomer counts (average elution volume of fraction given). The experiments were repeated with unlabeled monomer and no seeds or unlabeled seeds, and 1-mL fractions collected during elution from the Superdex 75 column were concentrated by lyophilization, dissolved in 8 M urea, and applied to a PVDF membrane for semiquantitative analysis using 6E10 primary antibody (Signet) and alkaline phosphatase-conjugated rabbit anti-mouse secondary antibody (Dako). The centers of the fractions shown in the eight dots in Fig. 4*B* correspond to elution volumes of 5.2, 6.6, 8.0, 9.5, 10.8, 12.2, 13.6, and 15.2 mL.

Cytotoxicity and Cell Viability Assays. Assays were performed on SH-SY5Y human neuroblastoma cells cultured under standard conditions at 37 °C in a humidified incubator with 5% CO_2. Cells were seeded at a density of 25,000 per well in a white-walled, clear-bottomed 96-well plate and cultured for 24 h in DMEM/10% FBS. The culture media were then replaced with prewarmed phenol red free DMEM without serum into which the peptide samples or $NaPO_4$ buffer were diluted 1:4. The peptide samples were taken directly from an ongoing seeded or unseeded aggregation reaction and subjected to filtration through a 200-nm filter (Anapour). Control peptide, monomer, and fibril were not filtrated. Buffer controls were both filtrated and unfiltrated. The cells were then cultured in the presence of the peptides, buffer, or media for a further 24 h before the cytotoxicity and viability assays were performed. Caspase-3/7 activity was measured using the Apo-ONE Homogeneous Caspase-3/7 assay (Promega). The fluorogenic caspase-3/7 substrate was diluted 1:100 in the lysis buffer provided and added to the cell medium at a 1:1 ratio. The reagent/cell mix was then incubated for 1 h before measuring the fluorescence at excitation 480 nm/emission 520 nm in an Optima FluoStar plate reader. Cell viability was measured using the Cell Titer 96 Aqueous One MTS reagent from Promega. The MTS reagent was added to the cell culture medium and incubated with the cells at 37 °C in a humidified incubator with 5% CO_2 before the absorbance at 495 nm was measured in an Optima Fluostar plate reader. All values given for both assays are buffer subtracted. The reduction in viability was calculated as the percentage reduction in MTS signal (absorbance at 495 nm) for each sample compared with that of the buffer-treated cells.

Theoretical Analysis

Global Analysis of Experimental Kinetic Data. The time to half-completion of each curve was determined by extracting from the experimental profiles the data points corresponding to a fractional fibrillar mass concentration value of between 0.4 and 0.6 and then performing a linear regression of these data points. The resulting straight-line fit was used to determine the time to half-completion for every individual curve, and the mean and SE were then found for each concentration (Fig. 2 *A–E*, *Lower*). The scaling exponent was found by a nonlinear fit of a power-law relationship, $\tau_{50\%} = \beta m(0)^{\gamma}$, for β, γ to these half-time data, weighted inversely by the square of the SEs of the data at each concentration. The scaling relationship observed at quiescent conditions is shown in Fig. S3*A* over an extended range of concentrations in comparison with Fig. 1*A*.

The two-parameter quiescent global fit in Fig. 1*D* was performed using the analytical rate law presented in our previous analysis (4), Eq. **1**, for the time evolution of a polymerization reaction in which the dominant mechanism is a monomer-dependent secondary nucleation process. The single-parameter global fits in Fig. 2 were performed using an analytical solution for the case where both fragmentation and monomer-dependent secondary nucleation mechanisms are considered, given as Eq. **1** with redefinitions of $\kappa = \sqrt{2k_+ m(0)[k_2 m(0)^2 + k_-]}$ and $k_\infty = \kappa\{2/[(-2\gamma-1)((-2\gamma-1)+1)]+2\lambda^2/[n_c\kappa^2]\}^{1/2}$, where γ is the experimental scaling exponent observed in each case (−0.94, −0.76, −0.66, and −0.62 from Fig. 2). In these fits the rate constants found in the analytical global fit in Fig. 1*D* were fixed to these predetermined values, leaving only one free kinetic parameter, k_+k_-. The final single-parameter fit in Fig. 2*E* was also performed using the analytical result in ref. 4 for a system proliferating solely through aggregate fragmentation, yielding an identical result. All global analytical fits were carried out using a Levenberg–Marquardt algorithm.

Relating Scaling Exponents to Mechanisms. Information regarding the dominant mechanisms was inferred from the scaling exponents based on our previous analysis (4–6). In particular, a powerful example of the dominance of the two principal parameters λ and κ is given by the power-law behavior $\tau_{50\%} \sim m(0)^{\gamma}$ that relates the half-time, $\tau_{50\%}$, at which half of the total peptide is present in aggregated form, to the initial peptide concentration $m(0)$; the exponent γ in this power law is to a good approximation given by $\gamma = -n_c/2$ for processes where the primary nucleation step is the major source of oligomers and by $\gamma = -(n_2+1)/2$ for phenomena where secondary nucleation processes dominate (4–7). The lag time before the observation of aggregates follows the same scaling behavior; we use here the half-time because it is available accurately from experimental data. A strong overall monomer dependence in Table 1 refers to the possibility, but not a guarantee (8), of a scaling exponent $|\gamma| \geq 1$, whereas a weak dependence refers to a scaling exponent $|\gamma| < 1$ (4–6).

The value for the scaling exponent measured in Fig. 1*A* and Fig. S3*A* for Aβ42 under quiescent conditions is -1.33 ± 0.03. In addition, the data in Fig. S3*B* show that the same value for the scaling exponent is observed even when a small amount of preformed fibrils is added at the beginning of the reaction to bypass primary nucleation (7), indicating that primary nucleation does not make a large contribution to the observed monomer scaling. It is interesting to note that these observations exclude aggregate

fragmentation, believed to be vital in the propagation of prions, as the dominant mechanism driving Aβ42 aggregation, because this process would result in an exponent of $\gamma \lesssim -0.5$ as it corresponds to a monomer-independent secondary pathway, $n_2 = 0$. The value of the scaling exponent observed is, however, consistent with a dominant secondary nucleation pathway characterized by a monomer dependence of $n_2 = 2$ and a minor contribution from primary nucleation, the effect of which is to lower the magnitude of the scaling exponent (4–7) from the value $\gamma = -(n_2 + 1)/2 = -1.5$ toward the value given for proliferation through primary nucleation only, $\gamma = -1$ for $n_c = 2$; the addition of preformed fibrils at the beginning of the reaction results in a similar minor reduction in the magnitude of the scaling exponent below $\gamma = -1.5$ (5, 9). We directly confirm this conclusion by checking explicitly in Fig. 1*D* the high degree to which the experimental data determined for the full time course of the reaction are matched by the predictions from the rate law, Eq. **1**, when all 10 initial peptide concentrations are used and the only two free parameters, $\sqrt{k_+k_n}$ and $\sqrt{k_+k_2}$ that enter κ and λ, are fixed globally to the same values for all 10 measured peptide concentrations to provide the best fit for the entire dataset.

Having established the mechanism of aggregation for Aβ42 at quiescent conditions, the rate equations (4) predict that, if fibril fragmentation is gradually introduced as a molecular mechanism for Aβ42 in addition to the processes already found under quiescent conditions, the scaling exponent will move from the quiescent value of −1.33 toward −0.5, as fragmentation gradually becomes the dominant process driving the creation of new Aβ42 aggregates. The experimental results acquired in the presence of increasing shear forces, shown in Fig. 2, reveal that the data display clearly this predicted feature: the half-time scaling exponent, given by the slopes in Fig. 2, *Lower*, is altered monotonically from -1.33 ± 0.03 (quiescent) to -0.62 ± 0.04 (agitation rate at 600 rpm), in excellent agreement with the theory and approaching the theoretical limit (4–6) of −0.5 at very high shear.

Fits to Alternative Mechanisms at Quiescent Conditions. ***Primary nucleation.*** The global fit in Fig. 1*B* is to the classical Oosawa theory of nucleation polymerization (10, 11), which is recovered to leading order by Eq. **1** when the rates of the secondary pathways are set equal to zero (5, 6). In this case, the scaling behavior that is observed for the half-time, Fig. 1*A*, can be best accounted for by a primary nucleation exponent of around $n_c = 3$, leaving the single combined rate parameter k_+k_n that controls proliferation through primary nucleation and growth to be fitted globally, resulting in the fit shown in Fig. 1*B*. It is clear that although the scaling behavior of the half-time is approximately recovered, the model cannot even qualitatively describe the kinetic reaction time courses observed.

This result is in agreement with the kinetic data in Fig. 4*D*, which point in a model-independent manner to the dominant role of secondary pathways, rather than primary nucleation, in generating most new aggregates (7). When preformed fibrils are added at the beginning of the reaction in Fig. 4*D*, the kinetic profile (dark blue) goes toward completion before the corresponding reaction without preformed fibrils (light blue) has generated significant aggregate mass; in particular, the rapid increase in the slope of the assay with preformed fibrils (dark blue) after *ca*. 15 min indicates rapid creation of new aggregates (7). The matched profile without preformed fibrils (light blue) shows that primary nucleation is not rapidly creating new aggregates at this time, and by definition the addition of fibrils cannot affect primary nucleation, pinpointing the origin of the new aggregates as the effect of secondary pathways (7). The radiocounting experiments shown in Fig. 4*A* provide independent evidence for this conclusion.

Fragmentation. If the fragmentation rate is allowed to vary in addition to the primary nucleation rate, but with the secondary nucleation rate set equal to zero, the best fit of the model (4) to the kinetic data corresponds to a system where most new aggregates are still created through primary nucleation, but where fragmentation is active as a minor mechanism. This result is inconsistent with the data in Fig. S3*B*, where it is observed that primary nucleation does not make a large contribution to the monomer scaling. Moreover, the resulting fit does not accurately capture the characteristic shapes of the reaction profiles at early and late times, which are hallmarks of a secondary nucleation process (7). Furthermore, a model with only a minor contribution from a secondary pathway is inconsistent with both the kinetic data in Fig. 4*D* (as explained in *Fits to Alternative Mechanisms at Quiescent Conditions, Primary nucleation*) and with the radiocounting experiments in Fig. 4*A*, which both demonstrate that a secondary pathway is active as the dominant, rather than a minor, mechanism.

Because a global fit to a model where both primary nucleation and fragmentation are active results in a situation where fragmentation is a minor, rather than a dominant, mechanism, an additional constraint was added to generate a representative fit to the data in Fig. 1 for the model where fragmentation is the dominant mechanism that is generating new aggregates. Specifically, we enforced $k_+k_n = (10^3 \mathrm{M}^{-1})k_+k_-$, which corresponds to fragmentation becoming the dominant mechanism once the aggregate mass concentration reaches around 10 nM. The resulting fit is shown in Fig. 1*C*, where it is clear that neither the shape of the reaction profiles nor the scaling exponent, which in a system dominated by fragmentation (5, 6) is ~ -0.5, can be recovered by a model that describes the situation where filament fragmentation is the dominant mechanism responsible for generating new aggregates. This is in agreement with the radiolabeling experiments shown in Fig. 4*A*, where it is observed that the oligomers formed through the secondary process are generated from monomeric peptide (i.e., through secondary nucleation) and not from existing aggregates (i.e., through fragmentation), hence providing independent verification that fragmentation is not the dominant mechanism generating oligomers.

Predicted Change in Scaling Exponent Observed at High Monomer Concentration. The reduction in the half-time scaling exponent with increasing shear, identified in Fig. 2 *A–E* (*Lower*) and summarized in Fig. 3*B*, stems qualitatively from the fact that growth in a system driven by a monomer-dependent nucleation process has a higher dependence on the monomer concentration relative to growth in a system fragmenting under shear. A further prediction of the theory (4–6), therefore, is that at high monomer concentrations, fragmentation will become relatively less important in determining the growth kinetics if monomer-dependent nucleation processes are active. This feature emerges experimentally in the form of a deviation from the power-law relationship between the half-time and the peptide concentration at the highest concentrations used in this study. These data points are shown as open circles in Fig. 2 *A–E* (*Lower*) and Fig. S3*B* and fall markedly below the best-fit lines that describe the rest of the data at lower concentrations. Indeed, if the four best-fit lines in Fig. S3*B* that correspond to aggregation under external shear (red, orange, green, and blue) were to be extended to higher concentration, they would cross the best-fit line given from measurements of aggregation under quiescent conditions (extended purple line). This would correspond to a physically impossible situation because shear cannot slow down the polymerization reaction. Instead of following this nonphysical trend, the data indicate a change in exponent as a function of concentration that has the effect of reducing the half-times for the reactions under shear to values below the best-fit lines, such that the datasets thereby avoid, as the initial monomer concentration is increased, crossing each other or the best-fit line obtained under quiescent conditions. More specifically, the theoretical analysis shows that at high monomer concentrations all of the power-law relationships in Fig. S3*B* must become parallel to the

scaling law corresponding to that for the quiescent system. Very generally, these results highlight the close connection between the scaling exponent and the molecular mechanism of filaments growth, with a change of exponent being a hallmark of a change in molecular mechanism.

Scaling Exponent Does Not Originate from Primary Nucleation. To verify that the monomer scaling exponent that we measured at quiescent conditions does not contain a large contribution from primary nucleation, we performed experiments where primary nucleation was bypassed (7) through the addition of a small amount of preformed fibrils. The monomer scaling exponent observed under these conditions (Fig. S3*B*) is the same as that observed in the absence of seed material (Fig. S3*A*). These experiments show that primary nucleation does not contribute a significant part of the monomer scaling. This experimental result eliminates the possibility that the monomer scaling exponent at quiescent conditions emerges from proliferation involving filament fragmentation and a significant contribution from primary nucleation with a large nucleation exponent n_c, which could increase the magnitude of the scaling exponent from the fragmentation-dominated limit, $\gamma = -1/2$, significantly toward the value given for primary nucleation alone, $\gamma = -n_c/2$. For this type of mechanism, the scaling exponent would revert to the value for a fragmentation-dominated system, $\gamma = -1/2$, when primary nucleation is bypassed, in contradiction to the experimental data for the case where preformed fibrils are added at the beginning of the reaction (Fig. S3*B*). By contrast, the monomer-dependent secondary nucleation mechanism is fully consistent with the data in Fig. S3. Note that a minor reduction in the magnitude of the scaling exponent below $\gamma = -1.5$ is also observed in the presence of preformed fibrils (Fig. S3*B*), in agreement with the predictions of the kinetic theory (5, 9).

Fibril Morphology Is Similar at All Shear Rates. We observed experimentally that the fibril morphology is similar at the different shear rates under which the reactions were carried out in Fig. 2. Using electron microscopy (Fig. S4), no fibrils were found at zero time (consistent with the isolation of monomer just before starting the experiment). Fibrils were found in all other samples, i.e., taken at 15, 30, and 45 min into the lag phase and after reaching the equilibrium plateau. The fibrils found under all conditions are remarkably similar (Fig. S4): typically, fibrils with a diameter of the order of 10 nm are seen. A greater prevalence of short fibrils is observed at higher shaking speed, but some very long fibrils are seen at all levels of shear. The average length at quiescent conditions is expected to be of the order (4, 12) $\delta k_+ m(0)/\kappa \approx 1\mu$m, consistent with observations here, and calculated using the rate constants determined in the main text with an extension $\delta \approx 1$Å per monomer (13, 14).

Furthermore, we carried out experiments to determine whether the kinetics of reactions seeded with fibrils formed at varying levels of shear differed. When preformed fibrils formed at different shaking speeds are added to monomeric peptide, the acceleration of the reaction is very similar in all cases (Fig. S5). In particular, through adding high concentrations of preformed fibrils formed at different shaking speeds to monomeric peptide (Fig. S5*A*), it is observed that the rates of elongation of fibrils formed at different levels of shear, which are proportional to the initial slopes of the reaction profiles (7), are very similar. Similarly, adding low concentrations of seed material to monomeric peptide (Fig. S5*B*) reveals that fibrils generated at different levels of shear promote secondary nucleation very similarly.

Acceleration Through Seeding Is Due to Fibrils and Not Oligomers. To determine whether the acceleration of the reaction that we observed upon addition of preformed aggregate material to monomeric peptide in Fig. 4*D* is due to preformed fibrils or oligomers, we performed control experiments (Fig. S6) where the preformed aggregate material is filtered before being added to monomeric peptide. When the filtrate (<200 nm) is added to monomeric peptide, significant acceleration is not observed (Fig. S6*C*); when the retentate (>200 nm) is added to monomer peptide, the reaction is accelerated in the same manner as when the unfiltered preformed aggregate material is used (Fig. S6*B*). These experiments verify that it is fibrils (larger than 200 nm, consistent with the TEM images in Fig. S4), rather than oligomers, that are primarily acting to accelerate the reaction.

Experimental Measurements of Aβ42 Aggregate Concentrations from Patients with Alzheimer's Disease and Control Subjects. Experimental measurements of Aβ loads in patients with Alzheimer's disease (AD) and age-matched control subjects were collated from the literature and are shown together in Table S1. Table S2 shows the median and the upper and lower quartiles for the patients with AD and the healthy controls from this collated dataset.

Six of these studies (15–20) reported values for insoluble Aβ1–42, whereas two reported values for insoluble Aβx–42 (21, 22), and two reported values for only total insoluble Aβ (23, 24). The studies (15–20) where concentrations for soluble and insoluble Aβ40 and Aβ42 were reported individually suggest that a measurement of total insoluble Aβ would be equal to within an order of magnitude of the concentration of insoluble Aβ42, and so these values are included in the analysis (Table S1). Three of the studies (16, 21, 22) reported values for multiple brain regions; the individual concentrations reported generally differ by less than one order of magnitude, and so an average is reported in Table S1. In cases where some of the control subjects displayed aggregate loads below the stated detection threshold (18, 19), the threshold value itself was used as the Aβ42 concentration, resulting in an overestimate for the aggregate loads in these control subjects in this analysis.

The measurements in each study were made using varying extraction and immunoassay techniques. Despite the spread in reported values across the different measurements, the collated dataset described in Tables S1 and S2 establishes a broad view of the concentration of aggregated Aβ42 in control subjects and patients with AD. It is interesting to note in particular that the concentration of Aβ42 aggregates observed in the brains of patients with AD is on average two orders of magnitude above the critical concentration of aggregates (*ca*. 10 nM) where, in our study, secondary nucleation became more important than primary nucleation in creating new oligomers.

1. Walsh DM, et al. (2009) A facile method for expression and purification of the Alzheimer's disease-associated amyloid beta-peptide. *FEBS J* 276(5):1266–1281.
2. Hellstrand E, Boland B, Walsh DM, Linse S (2010) Amyloid β-protein aggregation produces highly reproducible kinetic data and occurs by a two-phase process. *ACS Chem Neurosci* 1(1):13–18.
3. Nilsson MR (2004) Techniques to study amyloid fibril formation in vitro. *Methods* 34(1):151–160.
4. Cohen SIA, Vendruscolo M, Dobson CM, Knowles TPJ (2011) Nucleated polymerization with secondary pathways. II. Determination of self-consistent solutions to growth processes described by non-linear master equations. *J Chem Phys* 135(6):065106.
5. Cohen SIA, et al. (2011) Nucleated polymerization with secondary pathways. I. Time evolution of the principal moments. *J Chem Phys* 135(6):065105.
6. Knowles TPJ, et al. (2009) An analytical solution to the kinetics of breakable filament assembly. *Science* 326(5959):1533–1537.
7. Cohen SIA, Vendruscolo M, Dobson CM, Knowles TPJ (2012) From macroscopic measurements to microscopic mechanisms of protein aggregation. *J Mol Biol* 421(2–3):160–171.
8. Flyvbjerg H, Jobs E, Leibler S (1996) Kinetics of self-assembling microtubules: An "inverse problem" in biochemistry. *Proc Natl Acad Sci USA* 93(12):5975–5979.
9. Cohen SIA, Vendruscolo M, Dobson CM, Knowles TPJ (2011) Nucleated polymerisation in the presence of pre-formed seed filaments. *Int J Mol Sci* 12(9):5844–5852.
10. Oosawa F, Kasai M (1962) A theory of linear and helical aggregations of macromolecules. *J Mol Biol* 4:10–21.
11. Oosawa F, Asakura S (1975) *Thermodynamics of the Polymerization of Protein* (Academic, Waltham, MA).

12. Cohen SIA, Vendruscolo M, Dobson CM, Knowles TPJ (2011) Nucleated polymerization with secondary pathways. III. Equilibrium behavior and oligomer populations. *J Chem Phys* 135(6):065107.
13. Smith JF, Knowles TPJ, Dobson CM, Macphee CE, Welland ME (2006) Characterization of the nanoscale properties of individual amyloid fibrils. *Proc Natl Acad Sci USA* 103(43):15806–15811.
14. Lührs T, et al. (2005) 3D structure of Alzheimer's amyloid-beta(1-42) fibrils. *Proc Natl Acad Sci USA* 102(48):17342–17347.
15. Bao F, et al. (2012) Different β-amyloid oligomer assemblies in Alzheimer brains correlate with age of disease onset and impaired cholinergic activity. *Neurobiol Aging* 33(4):825–, e1–e13.
16. Hellström-Lindahl E, Viitanen M, Marutle A (2009) Comparison of Abeta levels in the brain of familial and sporadic Alzheimer's disease. *Neurochem Int* 55(4):243–252.
17. Wang J, Dickson DW, Trojanowski JQ, Lee VM (1999) The levels of soluble versus insoluble brain Abeta distinguish Alzheimer's disease from normal and pathologic aging. *Exp Neurol* 158(2):328–337.
18. Funato H, et al. (1998) Quantitation of amyloid beta-protein (A beta) in the cortex during aging and in Alzheimer's disease. *Am J Pathol* 152(6):1633–1640.
19. Gravina SA, et al. (1995) Amyloid beta protein (A beta) in Alzheimer's disease brain. Biochemical and immunocytochemical analysis with antibodies specific for forms ending at A beta 40 or A beta 42(43). *J Biol Chem* 270(13):7013–7016.
20. Tamaoka A, et al. (1994) APP717 missense mutation affects the ratio of amyloid beta protein species (A beta 1-42/43 and a beta 1-40) in familial Alzheimer's disease brain. *J Biol Chem* 269(52):32721–32724.
21. Lue LF, et al. (1999) Soluble amyloid beta peptide concentration as a predictor of synaptic change in Alzheimer's disease. *Am J Pathol* 155(3):853–862.
22. Näslund J, et al. (2000) Correlation between elevated levels of amyloid beta-peptide in the brain and cognitive decline. *JAMA* 283(12):1571–1577.
23. Kuo YM, et al. (1996) Water-soluble Abeta (N-40, N-42) oligomers in normal and Alzheimer disease brains. *J Biol Chem* 271(8):4077–4081.
24. van Helmond Z, Miners JS, Kehoe PG, Love S (2010) Higher soluble amyloid beta concentration in frontal cortex of young adults than in normal elderly or Alzheimer's disease. *Brain Pathol* 20(4):787–793.

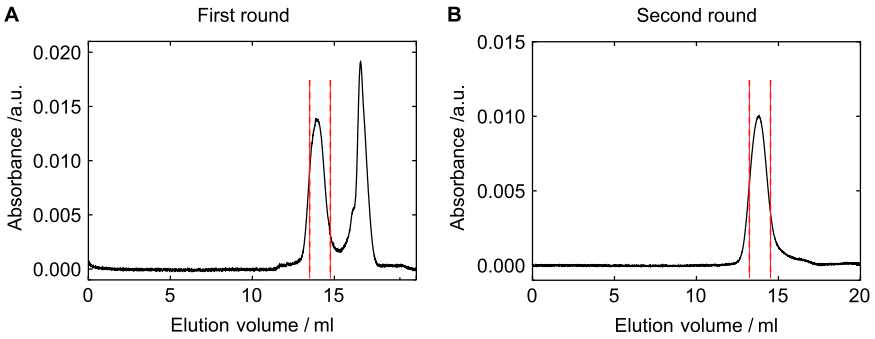

Fig. S1. Size exclusion chromatograms obtained during the multistep Aβ42 purification process used in these studies. (*A*) First round of purification where the monomer peak is initially selected (red dashed lines) and the second peak is mainly Tris and EDTA from the initial purification protocol (1). (*B*) This is followed by at least one further round of purification, wherein the center of the remaining monomer peak is selected (red dashed lines) to give the monomeric peptide to be used in studies.

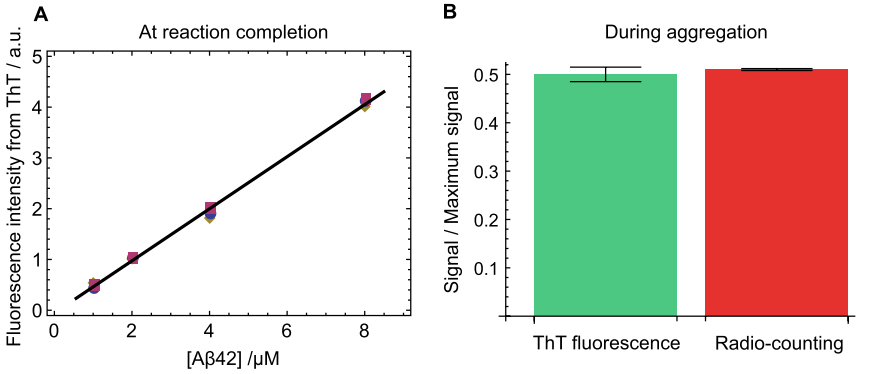

Fig. S2. Calibration of the relationship between fluorescence intensity from ThT and Aβ42 aggregate mass concentration. (*A*) Linear relationship between fluorescence intensity from ThT and that from total Aβ42 at reaction completion (here taken as the average fluorescence value between 10 and 12 h) where all of the monomeric peptide has been sequestered into aggregates (2). (*B*) Fraction of remaining free monomer measured by radiocounting at a time corresponding to the half-time as indicated by a ThT assay. The count of radiolabeled monomer shows that at the time reported by ThT as the half-time there is indeed precisely half of the monomeric peptide remaining in solution.

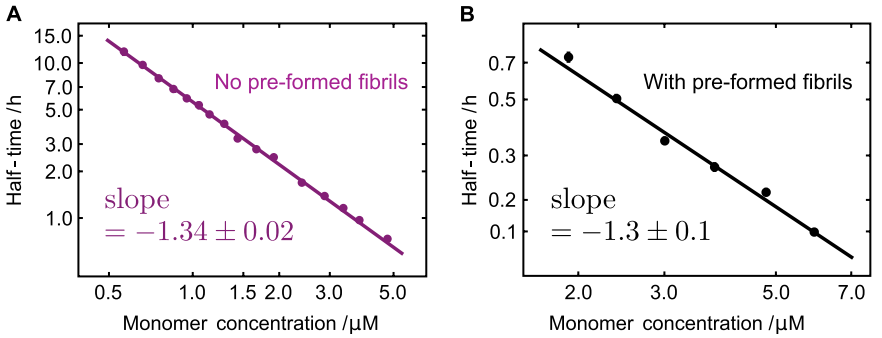

Fig. S3. (*A*) Power-law scaling relationship between the half-time, $\tau_{50\%}$, and the initial monomer concentration, $m(0)$, at quiescent conditions. The scaling exponent, $\tau_{50\%} \propto m(0)^{\gamma}$, over the extended range of concentrations shown here is $\gamma = -1.34 \pm 0.02$, consistent with the data shown in Fig. 1*A*. (*B*) Power-law scaling exponent between the half-time, $\tau_{50\%}$, and the initial monomer concentration, $m(0)$, for the case where 60 μM preformed fibrils is also added at the beginning of the reaction to bypass primary nucleation. The slope is the same as in *A*, indicating the monomer scaling exponent does not have a large contribution from primary nucleation.

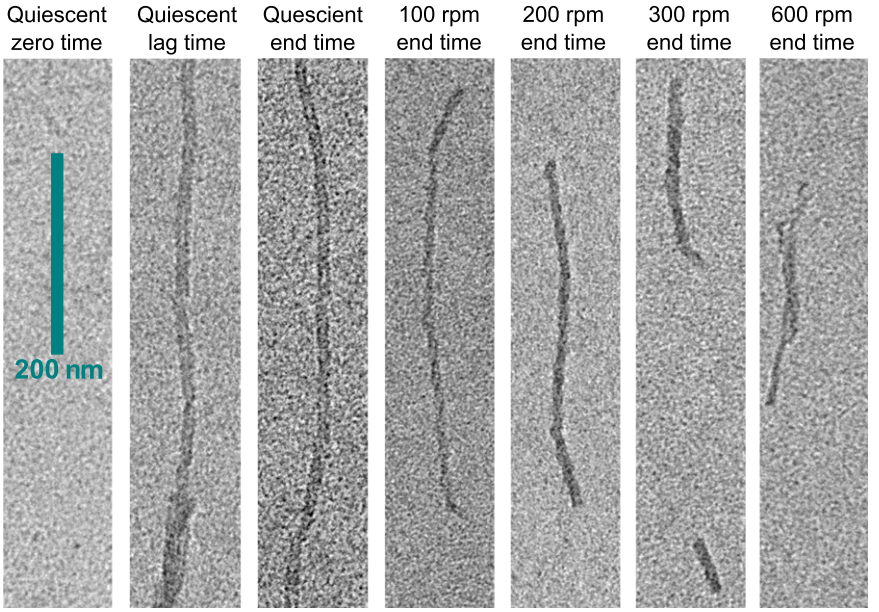

Fig. S4. TEM images of fibrils formed at different levels of shear (from *ca*. 3.4 μM Aβ42). The fibrils are all of similar morphology, with a shortening of the average length at higher shaking speeds. The average length at quiescent conditions is expected to be approximately (4, 11) $\delta k_+ m(0)/\kappa = 1$ μm, consistent with observations here and calculated using the rate constants determined in the main text with an extension $\delta \approx 1$ Å per monomer (12, 13). Fibrils are observed during the lag phase for all conditions, as expected (7). The end time refers to the time at which the plateau is reached in the reaction profile. No aggregates are observed at zero time.

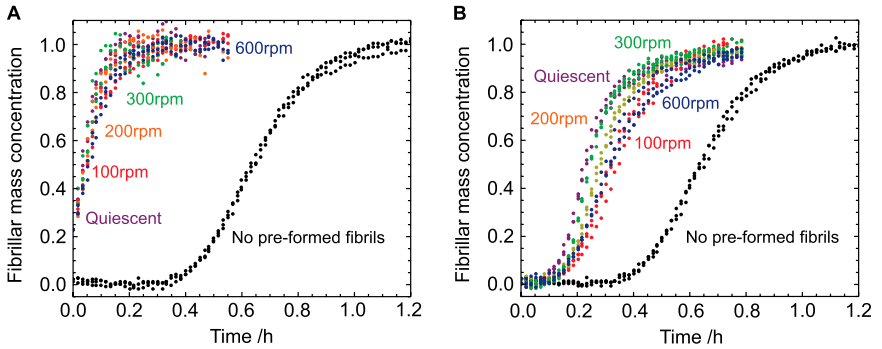

Fig. S5. Fibrils formed at different levels of shear accelerate the reaction very similarly. (*A*) Thirty percent (monomer equivalent) preformed fibrils formed at different shaking speeds (as annotated) are added to monomeric peptide (*ca*. 5 μM) at quiescent conditions. The initial slope, which is proportional to the elongation rate of the preformed fibrils (7), is very similar in all cases. (*B*) One percent (monomer equivalent) preformed fibrils formed at different shaking speeds (as annotated) are added to monomeric peptide (*ca*. 5 μM) at quiescent conditions. The resulting reaction profiles are very similar, indicating that preformed fibrils formed at each shaking speed are associated with very similar rates of secondary nucleation.

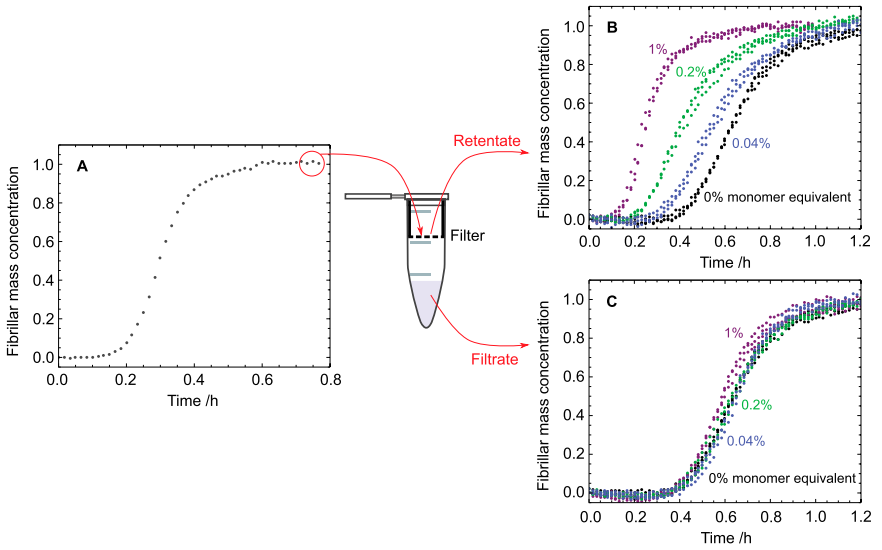

Fig. S6. Verification that the acceleration of the reaction observed upon the addition of preformed aggregate material is due to the addition of preformed fibrillar species rather than oligomers. An aggregation reaction (*ca*. 10 μM) is followed until completion, upon which the solution, as shown in *A*, is filtered through a 200-nm filter. (*B* and *C*) The retentate on the filter (*B*) and the filtrate (*C*) are added to monomeric peptide (*ca*. 5 μM). Only the retentate is observed to significantly accelerate the reaction. The concentrations of preformed aggregates in *B* and *C* are given as a percentage of the concentration of monomer peptide.

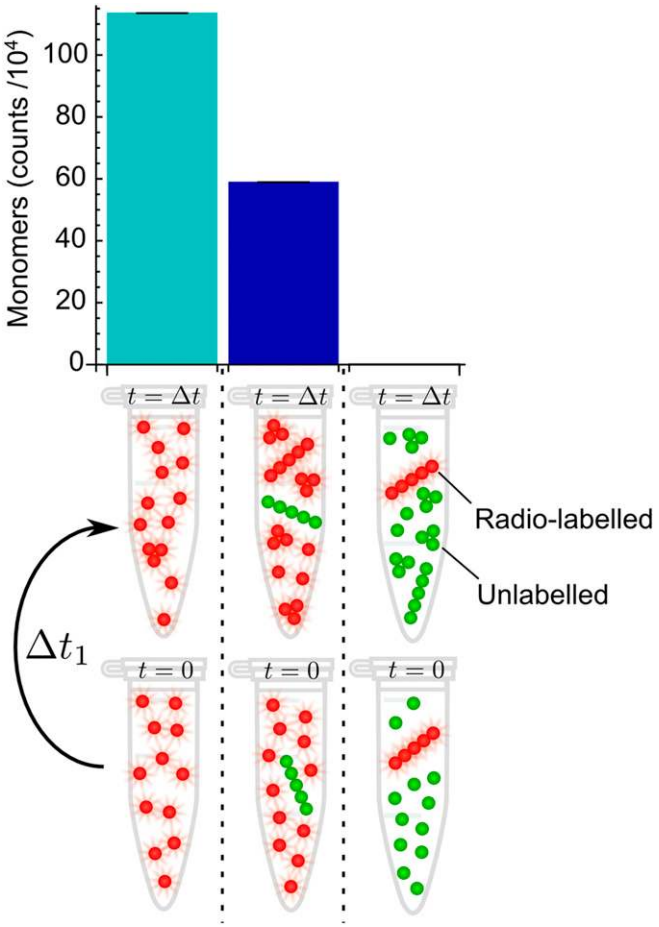

Fig. S7. Measurements of the monomer fractions for the same samples for which the oligomer fractions are shown in Fig. 4*A*, quantified by size-exclusion chromatography and selective radiolabeling. The ratio of the monomer concentration without (light blue bar) to that with (dark blue bar) preformed fibrils added is 2 at the measurement time, consistent with the kinetic data in Fig. 4*D*, because the sample without added fibrils (light blue bar) is still in the lag phase, whereas the sample with added fibrils (dark blue bar) has reached approximately the reaction half-time. The mass concentrations of oligomers in Fig. 4*A* are two orders of magnitude lower than the corresponding mass concentrations of monomers measured here. The combination of our ThT and radiolabeling measurements shows directly that, at the half-time of the reaction, approximately half of the protein mass remains in the monomeric state, approximately half is in fibrillar form, and only a small fraction is present as oligomers.

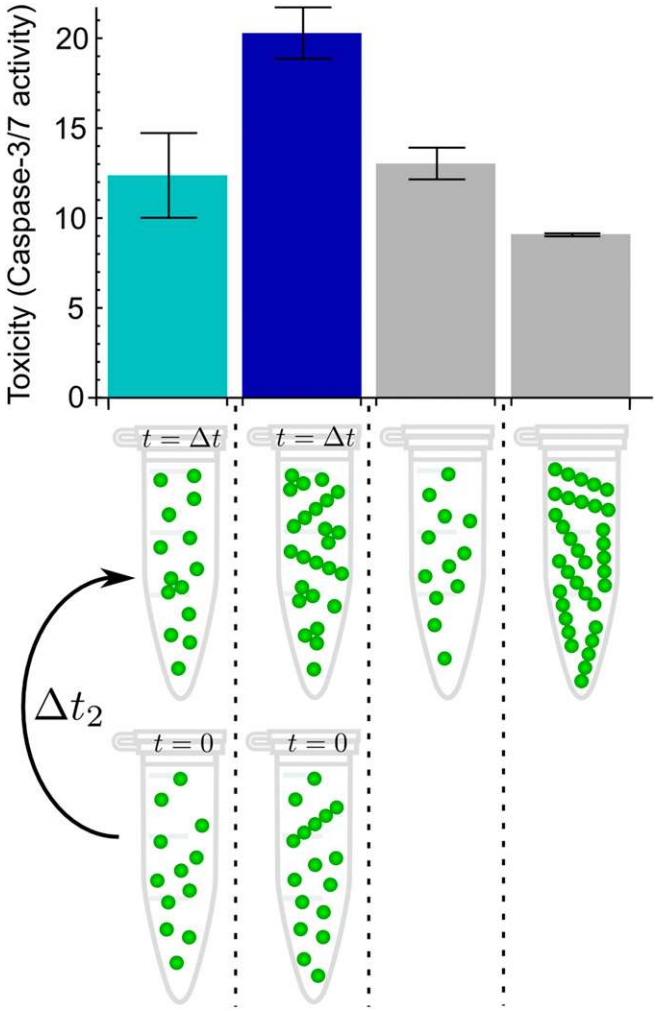

Fig. S8. Increase in cytotoxicity (caspase) was measured for reactions without (light blue bar) and with (dark blue bar) a small concentration of added preformed fibrils under the same conditions as the corresponding measurements of the decrease in cell viability (MTS) in Fig. 4*C*. In both assays, the highest toxicity is observed under conditions where the oligomer population generated through secondary nucleation is high.

Table S1. Literature values for the average Aβ42 aggregate load in patients with AD and control subjects

	Estimated Aβ42 aggregate load/nM	
Reference	Control subjects	Patients with AD
Bao et al. (15) [table 3]	40	2,000
Helmond et al. (24) [figure 1]	30	200
Hellstroem-Lindahl et al. (16) [figures 1 and 4]	20	200
Naeslund et al. (22) [table 2]	200	2,000
Wang et al. (17) [figure 4]	1	2,000
Lue et al. (21) [table 1]	2,000	30,000
Funato et al. (18) [figure 2]	10	6,000
Kuo et al. (23) [table 2]	2	200
Gravina et al. (19) [table 1 and text]	7	3,000
Tamaoka et al. (20) [table 1]	2	100

The specific source of the data within each reference is indicated in brackets. Values for the median and quartiles from this overall dataset are given in Table S2.

Table S2. Values for the median and the quartiles for Aβ42 aggregate loads calculated from the dataset shown in Table S1

	Estimated Aβ42 aggregate load/nM	
Quartile	Control subjects	Patients with AD
Lower quartile	2	200
Median	20	2,000
Upper quartile	40	3,000